



Citation for published version:

de O. Moraes, A, Vani, BC, Costa, E, Abdu, MA, de Paula, ER, Sousasantos, J, Monico, JFG, Forte, B, de Siqueira Negreti, PM & Shimabukuro, MH 2018, 'GPS Availability and Positioning Issues When the Signal Paths are Aligned with Ionospheric Plasma Bubbles', GPS Solutions, vol. 22, no. 4, 95, pp. 1 - 12.
<https://doi.org/10.1007/s10291-018-0760-8>

DOI:

[10.1007/s10291-018-0760-8](https://doi.org/10.1007/s10291-018-0760-8)

Publication date:

2018

Document Version

Peer reviewed version

[Link to publication](#)

This is a post-peer-review, pre-copyedit version of an article published in GPS Solutions. The final authenticated version is available online at: <https://doi.org/10.1007/s10291-018-0760-8>

University of Bath

General rights

Copyright and moral rights for the publications made accessible in the public portal are retained by the authors and/or other copyright owners and it is a condition of accessing publications that users recognise and abide by the legal requirements associated with these rights.

Take down policy

If you believe that this document breaches copyright please contact us providing details, and we will remove access to the work immediately and investigate your claim.

1 **GPS Availability and Positioning Issues When the Signal Paths are Aligned with**
2 **Ionospheric Plasma Bubbles**

3 **Alison de O. Moraes**

4 *Instituto de Aeronáutica e Espaço - IAE / Instituto Tecnológico de Aeronáutica - ITA*

5 São José dos Campos, SP, Brazil

6 alisonaom@iae.cta.br

7

8 **Bruno C. Vani**

9 *Instituto Federal de Educação, Ciência e Tecnologia de São Paulo - Campus Presidente*

10 *Epitácio (IFSP-PEP) /Universidade Estadual Paulista Júlio de Mesquita Filho - UNESP*

11 Presidente Epitácio, SP/ Presidente Prudente, SP, Brazil,

12 brunovani@ifsp.edu.br

13

14 **Emanoel Costa**

15 *Centro de Estudos em Telecomunicações, Pontifícia Universidade Católica do Rio de Janeiro*

16 *(CETUC/PUC-Rio), Rua Marquês de São Vicente 225, 22451-900 Rio de Janeiro, RJ, Brazil*

17 epoc@cetuc.puc-rio.br

18

19 **Mangalathayil A. Abdu**

20 *Instituto Tecnológico de Aeronáutica - ITA/Instituto Nacional de Pesquisas Espaciais – INPE,*

21 São José dos Campos, SP, Brazil

22 ma.abdu@inpe.br

23

24 **Eurico R. de Paula**

25 Instituto Nacional de Pesquisas Espaciais – INPE, São José dos Campos, SP, Brazil

26 eurico.paula@inpe.br

27

28 **Jonas Sousasantos**

29 *Instituto Tecnológico de Aeronáutica - ITA*

30 São José dos Campos, Brazil

31 jonasjss@ita.br

32

33 **João F. G. Monico**

34 *Universidade Estadual Paulista Júlio de Mesquita Filho - UNESP, Presidente Prudente, SP,*

35 *Brazil*

36 galera@fct.unesp.br

37

38 **Biagio Forte**

39 *University of Bath – Bath, United Kingdom*

40 B.Forte@bath.ac.uk

41

42 **Patrícia Mara de Siqueira Negreti**

43 *Instituto Nacional de Pesquisas Espaciais – INPE, São José dos Campos, SP, Brazil*

44 *São José dos Campos, Brazil*

45 patricia.mara@dae.inpe.br

46

47 **Milton Hirokazu Shimabukuro**

48 *Universidade Estadual Paulista Júlio de Mesquita Filho - UNESP*

49 *Presidente Prudente, SP, Brazil, miltonhs@fct.unesp.br*

50

Formatted: Portuguese (Brazil)

Formatted: Portuguese (Brazil)

Formatted: Portuguese (Brazil)

51
52
53
54
55
56
57
58
59
60
61
62
63
64
65
66
67
68
69
70

Formatted: Portuguese (Brazil)

Abstract The propagation paths of signals through equatorial ionospheric irregularities are analyzed by evaluating their effects on Global Navigation Satellite System positioning and availability. Based on observations during 32 days by a scintillation monitor at São José dos Campos, Brazil, it was noted that there is a dominance of enhanced scintillation events for Global Positioning System ray paths aligned with the azimuth angle of 345° (geographic northwest). This azimuth corresponds to the magnetic meridian that has a large westward declination angle in the region (21.4° W). Such results suggest that the enhanced scintillation events were associated with Global Positioning System signals that propagated along the direction of the magnetic field aligned plasma bubbles; in other words head-on through the plasma bubbles. It will be shown that, under this alignment condition, the longer propagation path length through plasma bubbles can result in more severe scintillation cases and more losses of signal lock, as supported by proposed statistics of bit error probability and mean time between cycle slips. Additionally, large precise positioning errors are also related to these events, as demonstrated by Precise Point Positioning experiments.

71 **Introduction**

72 Ionospheric scintillation degrades the accuracy of navigation and positioning based on Global
73 Navigation Satellite Systems (GNSS). Some authors observed that rapid phase variations are
74 mapped into Doppler shifts in the Global Positioning System (GPS) signal, which may exceed
75 the bandwidth of the phase lock loop, resulting in a loss of phase lock (Doherty et al. 2004).
76 Additionally, amplitude fades may cause the signal-to-noise ratio to drop below the receiver
77 threshold. These effects often accompany propagation delays and increase range measurement
78 errors, besides causing the carrier and code loops to lose lock (Kintner et al. 2001). Scintillation
79 may seriously affect positioning, resulting in total disruption of the receiver operation (Basu and
80 Basu 1981). Such extreme phenomena are more usual near the equatorial and low-latitude
81 regions (between $\pm 20^\circ$ geomagnetic latitude) than in the auroral and polar zones (above 55°
82 latitude). This work analyzes GPS scintillation data recorded during 32 days of the current solar
83 maximum conditions at São José dos Campos, Brazil (geographic coordinates: 23.2° S, 45.9° W,
84 dip latitude: 19.2° S), near the southern crest of the Equatorial Ionization Anomaly (EIA). The
85 analysis has been performed by relating the scintillation intensity with the geometry of the
86 propagation paths through the ionospheric irregularities and then evaluating the effects on GPS
87 positioning and availability. The nature of the plasma bubble irregularity distribution with
88 respect to the geomagnetic field configuration may magnify the scintillation effects. In Brazil,
89 the geomagnetic field configuration, characterized by a large magnetic declination angle,
90 provides a particular and favorable condition to assess such effects. A recent study by Moraes et
91 al. (2017) showed scintillation enhancement events around the azimuth angle of 345° , which
92 corresponds to signal propagation along ray paths that are nearly aligned with the magnetic
93 meridian in this region. In view of the large westward magnetic declination (21.4° W) of the
94 region, this result suggested that the enhanced scintillation events were associated with GPS
95 signals that propagated along the direction of the magnetic field aligned plasma bubbles.
96 Calculations of the propagation angles with respect to the magnetic field lines showed that small
97 values of this parameter and the larger propagation path length through bubbles could result in
98 severe scintillation and more cases of loss of phase lock. This analysis will also show that large
99 errors on Precise Point Positioning (PPP) are related to the eventual alignment.

100 Recently, Humphreys et al. (2009; 2010a) have suggested that deep fades in the
101 amplitude of received signals, simultaneously occurring with sudden phase changes, caused loss

102 of phase lock in carrier tracking loops of GPS receivers. Such occurrences, also known as
103 “canonical fades”, have been observed during strong low-latitude scintillation events
104 (Humphreys et al. 2010b). In the present work, the canonical fading will be examined as a likely
105 consequence of GPS signal propagation paths being aligned with the plasma bubble. These
106 nonlinear ionospheric propagation effects on the GPS radio signal will be analyzed using the
107 fading coefficients of the α - μ distribution (Yacoub 2007).

108 The next section will survey ionospheric scintillation. After a brief description of the
109 experimental setup, the period of analysis and the geophysical condition will be presented. In
110 sequence, a formulation that estimates the mean time between cycle slips in the receiver tracking
111 loop will be presented, based on its observed relation with the bit error probability (Humphreys
112 et al. 2010b). Next, the relation between scintillation parameters and propagation path directions
113 will be analyzed and evidences of the effects of this irregularity alignment on the GPS Precise
114 Point Positioning will be presented. The final section summarizes the main results in the study
115 and presents concluding remarks.

116

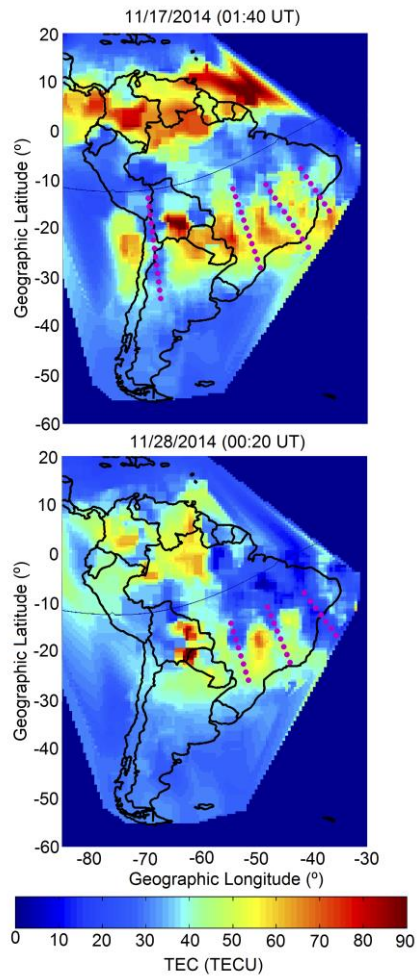
117

118 **The scintillation-producing ionospheric irregularities**

119 Plasma irregularities may develop in the post-sunset equatorial ionosphere under the
120 electrodynamic processes unique to the sunset transition. The pre-reversal enhancement in the
121 evening zonal electric field causes rapid uplifts of the steep gradient region of the bottomside
122 ionospheric F layer. This establishes the conditions for the interchange instability processes
123 driven by the Rayleigh-Taylor (R-T) mechanism to act on density perturbations, which begin to
124 grow. The nonlinear growth of the irregularities involves the bottomside lower density plasma
125 rising up even further to the topside ionosphere, in the form of magnetic flux tube aligned plasma
126 depletions (known as equatorial plasma bubbles, EPBs), with extremities extending to latitudes
127 of larger background plasma density in the Equatorial Ionization Anomaly. During their
128 evolution, the EPBs are observed to drift generally eastward. Motions of medium-scale density
129 secondary structures across transionospheric paths form complex moving field patterns at the
130 ground that contain amplitude and phase variations. In this way, random temporal fluctuations
131 are produced in both amplitude and phase of satellite signals received at the ground, which are

132 known as amplitude and phase scintillations, respectively (Yeh and Liu 1982). The irregularities
133 with scale sizes of a few hundred meters are responsible for producing scintillation of
134 transionospheric signals emitted by GNSS satellites (Kintner et al. 2007). Under geomagnetically
135 quiet conditions, the equatorial scintillation activity develops in the post-sunset hours and
136 typically lasts for 4-5 hours until midnight, sometimes also extending for a few hours into the
137 post-midnight period. It presents strong seasonal and longitudinal variations that are dependent
138 on the corresponding variations in the alignment between the sunset terminator and the magnetic
139 meridian, as well as on the availability of seeding sources (Abdu et al. 1981; Tsunoda 1985). In
140 the Brazilian region, scintillation activity extends from September to March and peaks around
141 December. In addition, short-term variability may occur due to upward propagating atmospheric
142 waves, sudden stratospheric warming episodes, and changes in solar and magnetic activities (de
143 Paula et al. 2015; Abdu et al. 2015).

144 EPBs have east-west extension of a few tens to hundreds of kilometers and often occur in
145 succession with zonal separation of a few hundred kilometers. Such features may be noted as the
146 magnetic north-south aligned depletion patches in the total electron content (TEC, with units of
147 10^{16} el/m²) distribution map constructed from measurements using GPS receiver arrays. Some
148 examples of such TEC maps over Brazil, using data from 17 to 28 November 2014, are shown in
149 Figure 1. Note that the TEC depletions (valley regions), associated with equatorial plasma
150 bubbles, extend from the EIA trough region (along the dip equator) to the EIA crest region of
151 (red and brown) larger background TEC values. We also note a large degree of day-to-day
152 variability in the TEC depletions, as well as in the background TEC values. Two situations lead
153 to intense scintillation. The first is the presence of the larger background plasma density that
154 exists in the crest region of the Equatorial Ionization Anomaly, where the plasma irregularities
155 are more intense. The second situation, which is the focus of the present study, is the degree to
156 which segments of signal propagation paths become closer to being aligned with the field-
157 aligned plasma bubble structures. Since scintillation results from effects integrated along the
158 propagation path, the longer the field-aligned propagation segment, the more intense will the
159 amplitude (or phase) scintillation be. In other words, the geomagnetic declination and inclination
160 angles associated with the GPS propagation path 350-km Ionospheric Pierce Point (IPP)
161 distribution are controlling factors of the scintillation distribution surrounding a receiving site.



162
 163 **Fig. 1** Examples of TEC maps over Brazil, showing the magnetic north-south aligned bubble
 164 structures (pink dots) with extremities extending several degrees to lower geomagnetic latitudes.
 165 Also shown are (red and brown) larger background TEC values in the EIA crest region.

166
 167

168 **Ionospheric scintillation measurements, spatial distribution and alignment**

169 The scintillation data used in the present study were recorded by a Septentrio PolaRxS monitor
170 belonging to the CIGALA/CALIBRA network (Vani et al. 2016). This monitor is located at São
171 José dos Campos (SJC), Brazil (geographic coordinates: 23.2° S, 45.9° W, dip latitude: 19.2° S).
172 The analysis focuses on two periods: 15-30 November 2014 and 04-18 February 2015. The
173 average sunspot number and the F10.7 solar flux values varied around 169 and 133 s.f.u. (1 s.f.u.
174 = 10^{-22} W/m²/Hz), respectively. The measurements were made during the equatorial spread F
175 occurrence season in Brazil, which typically extends from September to April (Sobral et al.
176 2002). For this study, GPS satellites with elevations greater than 20° were considered. In the set
177 of observations from 19:00 LT to 01:00 LT during 32 nights, approximately 179 hours of
178 significant GPS L1 amplitude scintillation were recorded, considering the transmissions from all
179 satellites.

180 The strength of the amplitude scintillation, represented by the S_4 index, defined as the
181 normalized standard deviation of the received signal intensity (Yeh and Liu 1982)

$$182 \quad S_4 = \sqrt{\frac{\langle I^2 \rangle - \langle I \rangle^2}{\langle I \rangle}} \quad (1)$$

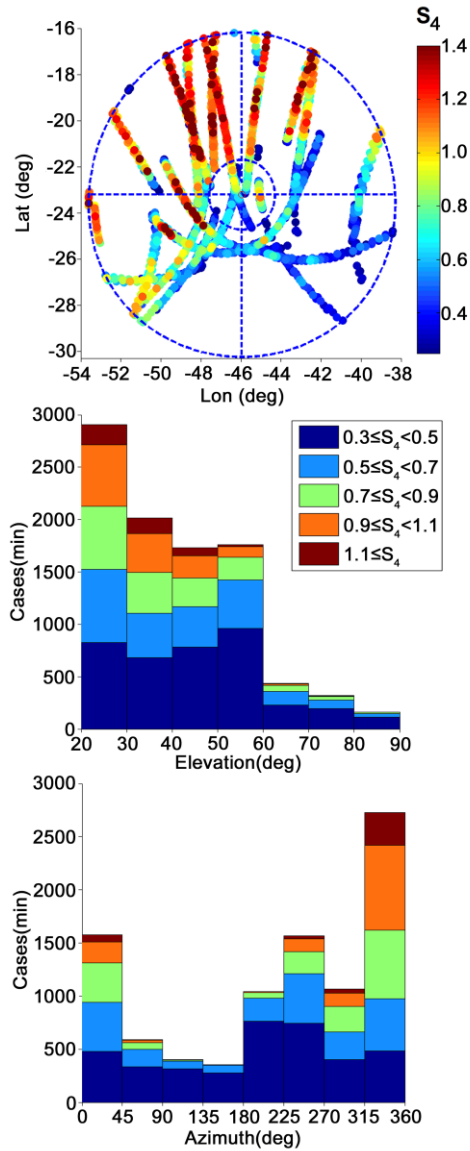
183 is one of the basic parameters for this study. In this well-known expression, $I = |R|^2$ is the
184 received intensity signal, R is its amplitude, and $\langle \rangle$ denote an ensemble average during one
185 minute. The receiver records the intensity at 50 Hz for all tracked satellites, providing the
186 respective S_4 index at every 60 seconds. Only samples with $S_4 > 0.3$ were considered as
187 scintillation cases. The first Fresnel zone scale sizes of the field-aligned irregularities that are
188 responsible for scintillation, immersed in the larger-scale plasma bubbles, are approximately
189 equal to 400 meters at the GPS L-band frequencies.

190 Figure 2 shows the azimuth and elevation distributions of amplitude scintillation
191 observed by the São José dos Campos monitor during the two periods of observations. All 10743
192 scintillation cases with $S_4 > 0.3$ were used in this plot. The top panel of Figure 2 shows azimuth-
193 elevation distribution of the S_4 values in association with the 350-km IPPs, using the color scale
194 on the right to represent the scintillation strength. Note that consecutive orbits show very small
195 day-to-day variations during the period of observation. To emphasize the severity of scintillation
196 effects on GPS transmissions, the highest S_4 values were brought to front in this plot, showing
197 the predominance of moderate-to-strong amplitude scintillation levels with $S_4 > 0.9$ in the

198 northern sector. This feature may be partly due to the ambient plasma density, since TEC must
199 be stronger in the northern sector over São José dos Campos, which includes the crest of the
200 EIA. Scintillation is highly dependent on the apex altitude of the irregularities. The apex
201 altitudes, corresponding to the aligned cases in the northern sector, vary from 431 km to 556 km.
202 Equatorial plasma bubbles commonly reach these apex altitudes over Brazil (Abdu et al. 2009).
203 In principle, bubble irregularities may also extend to regions southward of the receiving site.
204 However, only weak signatures of such bubble irregularities were observed in the available data
205 set.

206 The middle and bottom bar charts in Figure 2 represent the elevation and azimuth
207 distributions of scintillation occurrences for S_4 values varying from $0.3 \leq S_4 < 0.5$ to $S_4 > 1.1$.
208 Note that 80% of the cases with $S_4 \geq 1.1$ are associated with elevations less than 41° . For $0.9 \leq S_4$
209 < 1.1 and $0.7 \leq S_4 < 0.9$ and the same elevation interval, the corresponding percentages are 75%
210 and 73 %, respectively. The azimuth chart confirms in quantitative terms the predominance of
211 high S_4 values between azimuths 315° and 360° . For this azimuth sector, $S_4 \geq 1.1$, $0.9 \leq S_4 < 1.1$,
212 and $0.7 \leq S_4 < 0.9$ make up 68%, 62%, and 40% of the observed data, respectively. These results
213 are consistent with the ones provided by Xu et al. (2012).

214



215

216 **Fig. 2** GPS L1 amplitude scintillation events plotted at the respective IPP values (top panel). The
 217 outer and inner circles define elevations of 20° and 60°. The middle and bottom panels show S_4
 218 distributions as functions of elevation and azimuth, respectively.

219 **Cycle slips, bit error rate and α - μ model**

220 Humphreys et al. (2010b) showed that the bit error probability P_e for binary differential phase-
 221 shift keying (binary DPSK) transmissions and the mean time between cycle slips T_s are closely
 222 related by $T_s \approx T_b/P_e$, where $T_b = 0.02$ s is the GPS L1 bit duration. Based on this connection,
 223 and assuming a Ricean fading channel, they proposed a model for estimating the cycle slip rate
 224 as a function of scintillation intensity, the fluctuation speed, and the carrier power to noise power
 225 density ratio.

226 Based on the work of Yacoub (2007), Moraes et al. (2012; 2014a) used the α - μ model to
 227 provides a flexible and realistic description of the amplitude scintillation. The α - μ probability
 228 density function (pdf) of the amplitude envelope R of the received signal is given by

229
$$f_R(r) = \frac{\alpha}{\Gamma(\mu)} \frac{\mu^\mu}{\tilde{r}} (r/\tilde{r})^{\alpha\mu-1} \exp[-\mu(r/\tilde{r})^\alpha] \quad (2)$$

230 where $\alpha > 0$ is an arbitrary fading parameter, $\tilde{r} = [E(R^\alpha)]^{1/\alpha}$, and $\mu > 0$ is the inverse of the
 231 normalized variance of R^α ; that is, $\mu = E^2(R^\alpha)/\{E(R^{2\alpha})-E^2(R^\alpha)\}$. Additionally, $\Gamma(z)$ is the Gamma
 232 function of the argument z .

233 Based on the evidence provided by Humphreys et al. (2010b) and considering binary
 234 DPSK transmissions, P_e , and consequently T_s , will be estimated by using the α - μ model. To
 235 compute P_e , the α - μ probability density function (pdf) of the instantaneous signal-to-noise ratio
 236 $S = \tilde{s}(R/\tilde{r})^2$, where $\tilde{s} = \tilde{r}^2(E_b/N_o)$, and (E_b/N_o) is the energy per bit to noise power density
 237 ratio, is initially obtained from (2) by a straightforward derivation (Magableh and Matalgah
 238 2009)

239
$$f_s(s) = \frac{\alpha\mu^\mu}{2\Gamma(\mu)\tilde{s}} (s/\tilde{s})^{\alpha\mu/2-1} \exp[-\mu(s/\tilde{s})^{\alpha/2}] \quad (3)$$

240 Note that $(E_b/N_o) = T_b(C/N_o)$. Considering $E(R^2) = 1$, one gets

241
$$\tilde{r}^2 = \frac{\mu^{2/\alpha}\Gamma(\mu)}{\Gamma(\mu+2/\alpha)} \rightarrow \tilde{s} = \frac{\mu^{2/\alpha}\Gamma(\mu)}{\Gamma(\mu+2/\alpha)} (E_b/N_o) = \left[\frac{\mu^{2/\alpha}\Gamma(\mu)}{\Gamma(\mu+2/\alpha)} \right] T_b(C/N_o) \quad (4)$$

242 For binary DPSK, P_e is given by (El Ayadi and Ismail 2014)

243
$$P_e = \int_0^{\infty} \frac{1}{2} \exp(-s) f_S(s) ds \quad (5)$$

244 Combining (3) to (5) and changing the integration variable, P_e can be computed by

245
$$P_e = \frac{\alpha \mu^\mu}{4\Gamma(\mu)} \int_0^{\infty} v^{\alpha\mu/2-1} e^{-(\mu v^{\alpha/2} + \tilde{s}v)} dv \quad (6)$$

246 Several formulations for P_e calculation have generally adopted the moment generating function
 247 (MGF) approach to express their final results in closed forms, in terms of transcendental
 248 functions (Magableh and Matalgah 2009; El Ayadi and Ismail 2014). However, (6) may be
 249 easily and accurately calculated by numerical quadrature methods.

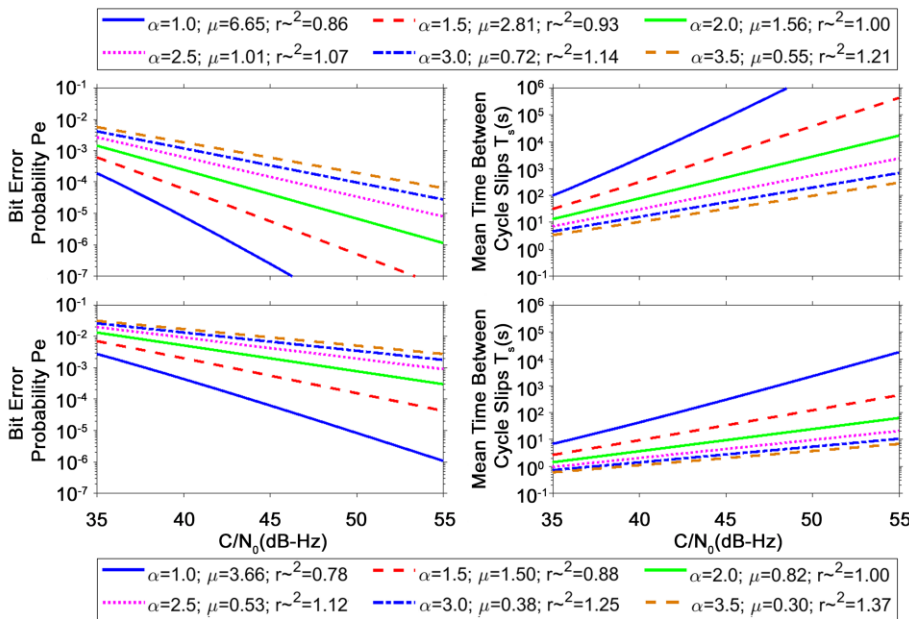
250 The left panels of Figure 3, obtained from (6) through the latter approach, illustrate the
 251 dependence of P_e as a function of C/N_o , for $S_4 = 1.1$ (upper left), $S_4 = 0.8$ (lower left), and
 252 different values of $(\alpha, \mu, \text{ and } \tilde{r})$. By using the α - μ model, it is more intuitive to analyze
 253 scintillation based on S_4 , having α as an auxiliary severity indicator. Indeed, Moraes et al.
 254 (2014b) established the following relation between the scintillation index S_4 and the parameters
 255 of the α - μ distribution

256
$$S_4^2 = \frac{\Gamma(\mu)\Gamma(\mu+4/\alpha) - \Gamma^2(\mu+2/\alpha)}{\Gamma^2(\mu+2/\alpha)} \quad (7)$$

258 This equation numerically leads to a μ value for each pair of independent parameters S_4 and α ,
 259 and the associated \tilde{r} value is immediately obtained from equation (4). Equation (7) indicates
 260 that the α - μ model may describe different scintillation patterns for each value of S_4 . This is
 261 especially interesting for strong scintillation, since it is well known that S_4 alone does not
 262 describe the effects from ionospheric perturbations on GPS signals. Each of the left panels of
 263 Figure 3 (with legends displaying, for fixed values of S_4 and selected α values, the calculated
 264 number for μ and \tilde{r}), confirms this information. As expected, the panels show that P_e decreases
 265 as S_4 increases and each curve shows that the bit error probability P_e decreases as C/N_o increases
 266 (and vice-versa). However, for $C/N_o = 42$ dB-Hz and $S_4 = 1.1$, the estimated values for P_e on the
 267 upper-left panel of Figure 3 are 2.1×10^{-4} , 3.8×10^{-3} and 1.4×10^{-2} , for $\alpha = 1.0, 2.0$ (the Nakagami-

269 m case) and 3.5, respectively. For $S_4 = 0.8$, the corresponding estimates on the bottom-left panel
 270 of Figure 3 are 2.0×10^{-6} , 1.3×10^{-4} , and 1.3×10^{-3} , for $\alpha = 1.0, 2.0$, respectively.

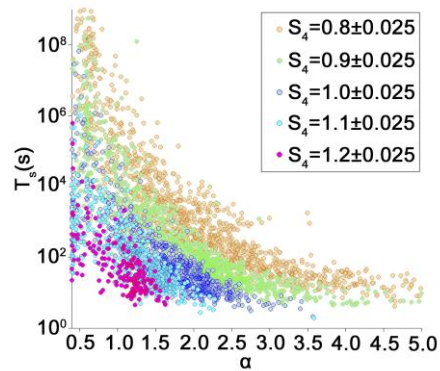
271 The right panels of Figure 3 simply map P_e into the mean time between cycle slips
 272 through the approximate relationship $T_s \approx T_b/P_e$. Correspondingly, these panels show that T_s
 273 decreases as S_4 increases and each curve shows that T_s increases as C/N_0 also increases (and
 274 vice-versa). It is also possible to observe the influence of S_4 , C/N_0 , and α on the cycle slip
 275 occurrence. Considering $C/N_0 = 42$ dB-Hz and $S_4 = 1.1$, the estimated values of T_s are 94.90 s,
 276 5.33 s and 1.48 s, for $\alpha = 1.0, 2.0$ and 3.5, respectively. For $S_4 = 0.8$, the corresponding estimates
 277 are 9.53×10^3 s, 1.61×10^2 s and 1.55×10^1 s. The above results illustrate how signals with similar
 278 S_4 and C/N_0 may have completely different effects on P_e and T_s .



279
 280 **Fig. 3** Curves for P_e (left panels) and T_s (panels) as functions of C/N_0 and different values of α
 281 (and associated values of μ and \tilde{r}). The upper and bottom panels assume $S_4 = 1.1$ and $S_4 = 0.8$,
 282 respectively.

Formatted: English (United States)

284 In addition to S_4 and average C/N_0 , the scintillation monitor records a flag indicating whether
 285 cycle slips occurred during the one minute of high-resolution (50 Hz) measurements. The
 286 estimated values of α , μ , P_e and T_s are also associated with each one-minute record. Figure 4
 287 displays the estimated T_s for the records in which cycle slips occurred, with each symbol
 288 representing the corresponding values of S_4 , α , and T_s . For a fixed value of S_4 (± 0.025), each
 289 scattered plot relates T_s to α , reinforcing that: (1) on average, T_s decreases with increasing values
 290 of S_4 ; and (2) for a fixed value of S_4 , an increase in α indicates an increase in the number of fades
 291 and an associated decrease in T_s (Moraes et al. 2014a). The observed dispersion in T_s for fixed
 292 values of S_4 and α is due to variations in C/N_0 . It should be remembered that the Septentrio
 293 PolaRxS GPS monitor is not a standard configuration. Instead, it is optimized for tracking
 294 through periods of scintillation. Thus, the above distribution of cycle slips is very likely different
 295 from those of normal GPS receivers in quantitative terms. However, it is expected that the
 296 qualitative principles extracted from the above results would also be applicable to them.
 297



298
 299 **Fig 4** Cycle slips detected by the scintillation monitor for different S_4 (± 0.025) ranges.

300

301

302 **Alignment and Availability**

303 This section associates P_e and T_s with the angle between the propagation path and the
 304 geomagnetic field directions. To obtain this angle, the propagation path direction lines (in terms

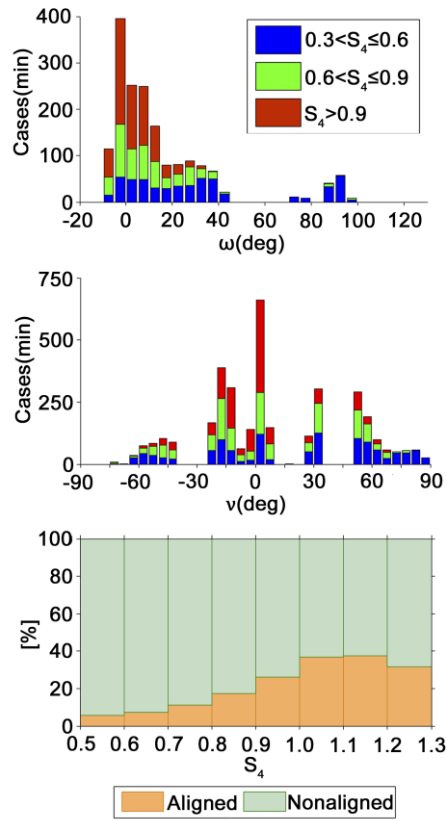
305 of their azimuth and elevation angles) at the 350-km IPPs were initially calculated for the
306 receiver location and all satellite positions at that moment. The latest version of the International
307 Geomagnetic Reference Field (*IGRF-12*) (Thébault et al. 2015) provided the geomagnetic field
308 line directions at the IPPs. Next, all determined lines were projected onto the vertical (north and
309 up) and horizontal (north and east) planes at the IPPs. The first projection (ω) measures the
310 difference between the path elevation and the geomagnetic inclination. Note that the path
311 elevations at the IPPs displayed by Figure 2, measured from the horizontal plane toward zenith at
312 the IPP, are always greater than 20° , as explained in the first paragraph of the third section.
313 Similarly, the geomagnetic inclination line is also above the same horizontal plane, since the dip
314 angle is negative in the southern hemisphere. However, the difference ω can be negative or
315 positive, indicating that the path elevation line is below or above the geomagnetic inclination
316 line, with respect to that horizontal plane, respectively. The second projection (v) represents the
317 angle between the path azimuth and the geomagnetic declination lines on the horizontal plane
318 through the IPP. While the path azimuths at the IPPs displayed by Figure 2 vary from 0° to 360° ,
319 the angle v can be negative, indicating that the path azimuth line is to the right of the
320 geomagnetic declination line, or positive, if the other relative position holds. Thus, the set of
321 parameters associated with each one-minute record, listed in the last paragraph of the previous
322 section, is augmented with ω and v . The present study assumed that if $|\omega|$ and $|v|$ are
323 simultaneously less than 10° , the GPS propagation path would be effectively aligned with the
324 ionospheric bubble irregularity structure.

325 The bar plots in the top and middle panels of Figure 5 display the number of L1
326 scintillation occurrences as a function of ω and v , for different ranges of S_4 . It is noted that the
327 smallest ω are related with the largest scintillation index interval, and vice-versa. Similarly, the
328 largest S_4 values occur when the difference between the propagation angle and the magnetic
329 declination is the smallest. Thus, a small angle between the propagation direction and the field-
330 aligned bubbles, on both vertical and horizontal planes, corresponds to large scintillation
331 intensity. The bottom panel of Figure 5 shows the percentages of aligned and nonaligned cases,
332 which always add to 100 % within each S_4 interval. It indicates that the increasing percentage of
333 alignment between the propagation angle and magnetic field line results in a severe increase of
334 the scintillation intensity.

335 The top panel of Figure 6 shows the estimated T_s values as functions of S_4 , where the
336 colors red and green represent aligned and nonaligned cases, respectively. It is noticed that the
337 aligned cases are concentrated in the region of high S_4 and low T_s values. The bottom panel in
338 Figure 6 shows the percentages of aligned and nonaligned cases for different T_s classes. Again,
339 the two percentages associated with each class add to 100 %. For very rare occurrences of cycle
340 slips ($48 \text{ h} < T_s \leq 168 \text{ h}$, corresponding to one such event within the interval from two days to
341 one week), the percentage of aligned cases is only 5.6%. This percentage increases to 18.5% for
342 T_s between 5 min and 20 min. However, for $1 \text{ s} < T_s < 10 \text{ s}$, the percentage of aligned cases
343 reaches 30.7%. Therefore, the alignment between the propagation path and the geomagnetic field
344 directions favors the occurrence of the most serious conditions for the GPS receiver operation,
345 leading to high values of S_4 and small values of T_s .

346

347

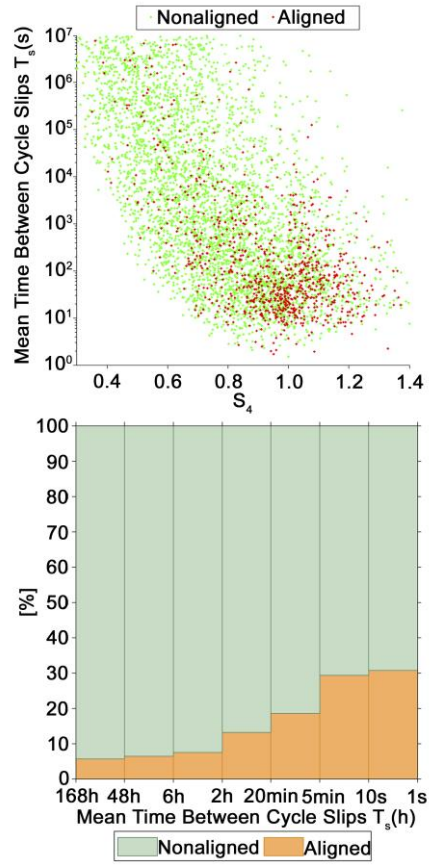


348

349 **Fig. 5** Top and middle panels: number of L1 scintillation occurrences as a function of ω and ν ,
 350 respectively, for different ranges of S_4 values. Bottom panel: percentages of alignment and
 351 nonalignment as functions of S_4 intervals. Note that, for all S_4 intervals, the two percentages
 352 always add to 100 %.

353

354



355

356

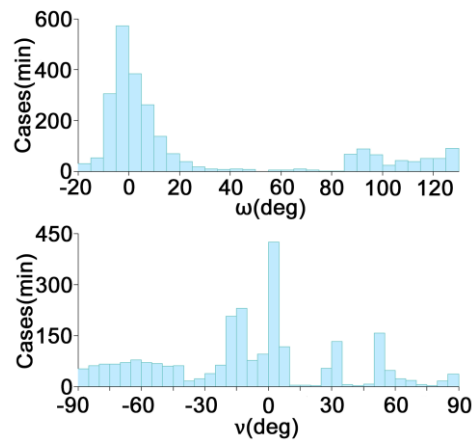
357 **Fig. 6** Top panel: scatter plot of the mean time between cycle slips T_s as a function of S_4 for of
 358 aligned and nonaligned cases. Bottom panel: percentages of aligned and nonaligned cases for
 359 different T_s classes. Note that, for all T_s classes, the two percentages always add to 100 %.

360

361 Figure 7 displays the histograms for ω and ν , conditioned by $T_s < 200$ s. They show the
 362 concentration of the most likely cases of loss of lock around 0° for both angles ω and ν . The
 363 percentages of S_4 classified by the alignment in Figure 5 and the present plots show that GPS
 364 signals received end-on through field aligned plasma bubbles may suffer enhancement in

365 scintillation intensity. In view of the inverse relationship between T_s and S_4 , evident in the top
 366 panel of Figure 6, the distributions of the numbers of cases of $T_s < 200$ s with respect to ω and ν ,
 367 which show their maximum occurrences at small angles, are consistent with top and middle
 368 panels of Figure 5. Such enhancement appears in addition to that occurring in the EIA crest
 369 region, arising from the fountain effect on the background plasma density. Scintillation
 370 enhancements due to the EIA crest region (to the north of the GPS receiver) may also contribute
 371 to the alignment effect seen on the vertical plane; that is, as a function of ω . However, the cases
 372 of enhanced scintillation intensity ~~and those of in which~~ $T_s < 200$ s for propagation alignment in
 373 azimuth ν do represent the scintillation enhancement for ~~end-on a case-view where unaff the eeted~~
 374 ~~by~~ EIA crest effect is smaller. Both effects make signal tracking more difficult, with direct
 375 impact on the performance and availability of GPS receivers.

376



377

378 **Fig. 7** Top panel: distribution of the angular difference between the path elevation and magnetic
 379 inclination (dip angle) for $T_s < 200$ s. Bottom panel: distribution of the value of the angular
 380 difference between the path azimuth and the geomagnetic declination for $T_s < 200$ s.

381

382 Table 1 presents the average and standard deviation values of α , as well as its maximum
 383 recorded value for different S_4 intervals, considering aligned and nonaligned cases. It also
 384 presents the number of analyzed cases in each class. The analysis considers only the one-minute

385 records affected by losses of lock, as indicated by the corresponding flag. It is observed that the
 386 average value of α for each aligned case is greater than the one for the corresponding nonaligned
 387 case. For all S_4 intervals, the increase of α values implies a decrease in the estimate of T_s as
 388 shown in Figure 3. This is an indication that the alignment affects the statistics of amplitude
 389 scintillation in a severe way, with distributions that display a higher percentage of deep fades
 390 than those related with the nonaligned ones (Moraes et al. 2014b).

391

392 **Table 1** Comparison between statistics of α coefficients for aligned and nonaligned conditions.

	Aligned				Nonaligned			
	E(α)	std(α)	max(α)	Cases	E(α)	std(α)	max(α)	Cases
0.3< S_4 ≤0.4	3.16	4.37	51.20	42	2.58	2.59	22.93	2151
0.4< S_4 ≤0.5	2.72	3.08	20.54	55	2.34	2.66	48.05	1549
0.5< S_4 ≤0.6	3.14	3.62	23.66	69	2.16	2.27	22.39	1176
0.6< S_4 ≤0.7	2.91	3.18	30.55	69	2.28	2.28	18.21	890
0.7< S_4 ≤0.8	2.83	2.70	22.16	91	2.21	1.67	13.74	733
0.8< S_4 ≤0.9	2.58	3.48	56.48	133	1.99	3.28	52.07	635
0.9< S_4 ≤1.0	2.01	1.09	12.38	188	1.82	3.13	43.86	534
1.0< S_4 ≤1.1	1.15	0.67	3.68	207	1.15	0.62	2.53	357
1.1< S_4 ≤1.2	1.02	0.48	2.20	100	0.90	0.44	1.68	166
1.2< S_4	0.81	0.37	1.62	57	0.65	0.34	1.40	123

393

394 This section showed that GPS signals propagating along the magnetic field lines are more
 395 likely to propagate longer distances in the turbulent medium created by the field-aligned EPBs.
 396 Therefore, the alignment geometry is more likely to cause interruptions to GPS receiver
 397 operation.

398

399 **Alignment and Positioning**

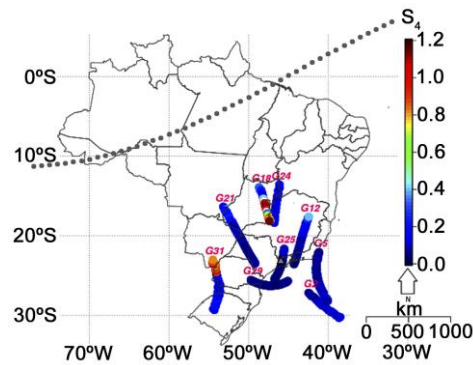
400 This section discusses the influence of ionospheric irregularity alignments with the signal
401 propagation paths on GPS positioning. The observation dataset was evaluated by the Precise
402 Point Positioning (PPP) approach (Zumberge et al. 1997) using the RT-PPP software developed
403 by the Universidade Estadual Paulista Júlio de Mesquita Filho (UNESP), available at <[http://is-
404 cigala-calibra.fct.unesp.br/ppp/](http://is-cigala-calibra.fct.unesp.br/ppp/)> (Marques 2014).

405 The PPP was applied with the standard configuration (that is, with corrections for
406 tropospheric and first-order ionospheric refraction effects, but without any attempt to mitigate
407 those from scintillation). Dual-frequency (L1 and L2) only GPS data were processed in the
408 kinematic mode, simulating real field conditions with a sampling rate of 1 s and elevation cutoff
409 of 10°. Within this mode, the position parameters and receiver clock error are estimated at every
410 epoch by the least-squares adjustment, while the phase ambiguities are estimated iteratively
411 (Marques et al. 2016). Typically, this procedure leads to centimeter-level accuracy within 20
412 minutes, due to the convergence period of the phase ambiguity parameters (Gao and Shen 2002).
413 In the presence of scintillation, PPP may experience higher-order errors mainly associated with
414 cycle slips and range degradations in the observables. Using the RT-PPP software, if a cycle slip
415 is detected through the algorithm designed by Blewitt (1990), its corresponding ambiguity
416 parameter is re-initialized. Consequently, a new convergence period is required for such
417 parameter and the accuracy of the positioning may deteriorate in the meanwhile. Another source
418 of deterioration in positioning accuracy is the sudden change in geometry caused by losses of
419 lock during scintillation, as highlighted by Zhang et al. (2014). The detection, identification and
420 adaption (DIA) method (Teunissen 1998) is applied for outlier detection and quality control
421 adjustment.

422 Typical examples of the influence of the alignment under discussion on the PPP
423 performance is presented in Figures 8 and 9, based on data recorded between 19:00 LT and
424 21:00 LT during the night of 17 November 2014. Figure 8 shows the skyplot of the time
425 variation of the IPPs of all available GPS satellite links to the São José dos Campos monitor, in
426 combination with the corresponding S_4 values. The satellite signals transmitted by PRN18 (G18
427 in the plot) are associated with ray paths aligned with magnetic-field elongated EPBs between

428 20:06 LT and 21:00 LT, being persistently and severely affected by the strongest scintillation.
429 However, the alignment condition actually started earlier at 19:35 LT, with little noticeable
430 effects.

431



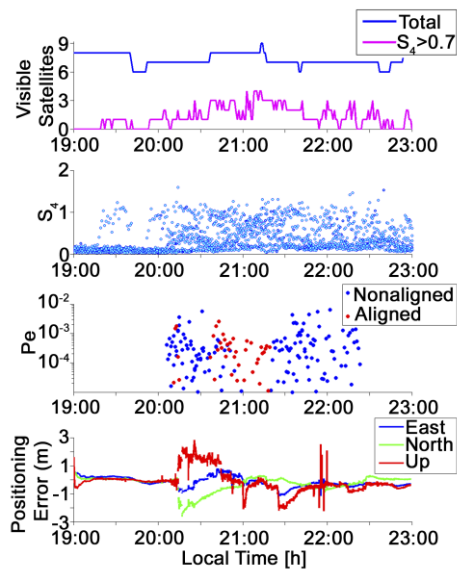
432

433 **Fig. 8** Skyplot of the time variation of the IPPs of all available GPS satellite links to the São José
434 dos Campos monitor in combination with the corresponding S_4 values for 17 November 2014
435 between 19:00 LT and 21:00 LT.

436

437 The upper three panels of Figure 9 present the total number of satellites used in the PPP
438 solution, S_4 values for all satellites, and the noticeable cases of bit error probability $P_e > 10^{-6}$ (T_s
439 < 20000 s). The bit error probability for the alignment condition, which only affected PRN18,
440 started at approximately 20:06 LT and lasted until 21:00 LT, being indicated by red dots.
441 However, the alignment precondition actually started at 19:35 LT, with lower P_e values. The
442 bottom panel of Figure 9 displays the time series of the North, East and Up PPP error
443 components. Analyzing the S_4 plot in Figures 9, it is observed that scintillation with $S_4 > 0.7$
444 started at 19:40 LT, so remaining until 21:00 LT, while the PPP solution experienced higher-
445 order errors, reaching (and sometimes exceeding) meter-level accuracy between 20:35 LT and
446 20:47 LT. These events occurred simultaneously with the period of EPB alignment with the
447 PRN18 propagation path, when noticeable values of P_e also occurred. This is an evidence that P_e
448 is a realistic parameter to diagnose difficulties in the PPP processing approach, not only under
449 alignment, where it is more perceptible, but also for $P_e > 10^{-6}$. What is quite relevant in the top

450 panel of Figure 9 is the fact that the transmissions by two satellites experienced simultaneous
 451 losses of lock during short intermittent intervals. These events are also identified by high P_e
 452 values, beginning at approximately 20:35 LT, according to corresponding panel of Figure 9. In
 453 the absence of adequate time for the PPP procedure to recover from losses of lock and converge
 454 again, its solution yields large errors.



455
 456 **Figure 9** – Example from 17 November 2014. From top to bottom: total number of visible
 457 satellites used by the PPP processing approach; all S_4 values estimated between 19:00 LT and
 458 23:00 LT; noticeable cases of bit error probability $P_e > 10^{-6}$ for aligned (red dots) and nonaligned
 459 cases (blue dots); and North (N), East (E) and Up (U) components of the positioning error
 460 calculated by the PPP processing approach.

461
 462 Table 2 presents detailed results from the highlighted night of 17 November 2014 (DOY
 463 321). It also presents observations for the period between 18 and 30 November, 2014. All
 464 alignment cases occurred for PRN18. The three-dimensional rms and average positioning error,
 465 calculated by the PPP processing approach, as well as its maximum value (all in m) are listed in

466 the last columns of Table 2, showing large PPP errors due to alignment. Such a result may be
467 considered for mitigation of this type error in the future.

468

469 **Table 2** PPP results under alignment conditions for 15-30 November 2014.

DOY	Cases $S_4 > 0.7$	Max(S_4)	Max(P_e)	RMS($3d\sigma$)	Max($3d\sigma$)	E($3d\sigma$)
321	30	1.28	0.0027	0.3623	2.0304	0.3770
322	26	1.19	0.0047	0.4130	1.9380	0.5791
323	48	1.37	0.0025	0.3241	2.5973	0.4232
324	0	0.45	0.0000	0.1077	0.8250	0.3982
325	51	1.60	0.0036	0.9226	2.8496	0.9686
326	34	1.25	0.0030	0.3528	2.5637	0.6211
327	43	1.22	0.0031	0.1888	1.2140	0.3040
328	63	1.21	0.0035	0.1100	0.6216	0.3685
329	52	1.41	0.0030	0.1020	0.6263	0.2716
330	31	1.31	0.0012	0.1573	1.5378	0.5249
331	46	1.33	0.0049	0.1996	1.2328	0.8322
332	12	1.00	0.0014	0.2643	1.2503	0.7543
333	8	1.06	0.0054	0.3266	2.3209	0.7251
334	20	1.27	0.0013	0.4386	2.4038	1.2289

470

471

472 **Conclusion**

473 DasGupta et al. (2004) and Ray et al. (2014) previously demonstrated that GPS signals are more
474 severely affected by scintillation when their propagation paths are aligned with EPBs. The
475 former reference based their arguments on azimuth-elevation plots of the scintillation index

476 estimated from measurements performed by a GPS monitor located at Calcutta (22.58°N,
477 88.38°E geographic; 32.19°N magnetic dip, 17.35°N dip latitude), as well as on corresponding
478 positioning errors, which reached 11 m in latitude and 8 m in longitude. The latter reference
479 displayed S_4 values along GPS satellite tracks observed from Bhopal (23.28°N, 77.34°E
480 geographic; 34.90°N magnetic dip, 19.20°N dip latitude) in combination with a map of the angle
481 between the ray path and the geomagnetic field directions, in terms of the subionospheric latitude
482 and longitude. Noting that the example also represented observations from several other stations
483 in the Indian sector, the authors also arrived at the above conclusion. Here, experimental data
484 obtained during 32 days at a station located under the Southern crest of the EIA in Brazil have
485 been analyzed. The results have confirmed that, in the Brazilian sector, scintillation intensity is
486 also enhanced when signal propagation path segments tend to align themselves with EPB
487 structures, which are known to be elongated along magnetic flux tubes. Such scintillation
488 enhancements occurred predominantly at azimuth angles around 345°, nearly aligned with the
489 magnetic meridian over this region, which has a large westward declination (21.4° W).
490 Moreover, that loss of phase lock is more likely to occur in the presence of this geometry. The
491 present scenario favors the assessment of such effects. To extend the previous results, statistical
492 analyses of the present experimental data have been performed. Next, the α - μ model has been
493 used to estimate the mean time between cycle slips T_s through its approximate relationship with
494 the bit error rate P_e of binary DPSK signals. Thus, it has been quantitatively shown that the
495 above alignment, which resulted in more severe scintillation cases with high values of S_4 , is also
496 responsible for small values of T_s , likely causing losses of phase lock. The Precise Point
497 Positioning analysis has shown that the large observed errors are related with that condition. The
498 results has shown that PPP also experienced significant errors for high values of P_e , even in the
499 absence of the alignment condition. In one particular example, these errors increased in response
500 to transmissions by two satellites experiencing simultaneous losses of lock during short
501 intermittent intervals. These events strongly impacted GPS availability and positioning
502 performance. However, it has been shown that such performance metrics have been specially
503 degraded under the alignment condition.

504

505

506 **Acknowledgements:** This work is supported by Conselho Nacional de Desenvolvimento
507 Científico e Tecnológico (CNPq) under award number (INCT) 465648/2014-2. B. C. Vani
508 thanks Federal Institute of Education, Science and Technology of Sao Paulo (IFSP) for
509 supporting his PhD research and Coordenação de Aperfeiçoamento de Pessoal de Nível Superior
510 (CAPES) for grant (CAPES/PDSE no. 19-2016/Process n. 88881.134266/2016-01). M. A. Abdu
511 acknowledges the CAPES support for a senior visiting professorship at ITA/DCTA. E. Costa is
512 supported by CNPq award number (PQ) 309013/2016-0. E. R. de Paula is supported by CNPq
513 award number (PQ) 310802/2015-6. The monitoring stations were deployed in the context of
514 Projects CIGALA/CALIBRA, funded by the European Commission (EC) in the framework of
515 FP7-GALILEO-2009-GSA and FP7-GALILEO-2011-GSA-1a, respectively, and FAPESP
516 Project Number 06/04008-2. The authors thank the reviewers for the insightful and constructive
517 comments, which helped them in the development of a better paper.

518

519 **References**

520 Abdu, M. A.; Bittencourt, J. A. Batista, I. S. (1981). Magnetic declination control of the
521 equatorial F region dynamo electric field development and spread F. *J. Geophys. Res.*, 86(13),
522 pp.11443–11446, doi:10.1029/JA086iA13p11443.

Formatted: Portuguese (Brazil)

523
524 Abdu, M. A.; Kherani, E. A.; Batista, I. S.; de Paula, E. R.; Fritts, D. C. Sobral, J. H. A. (2009).
525 Gravity wave initiation of equatorial spread F/plasma bubble irregularities based on
526 observational data from the SpreadFEx campaign. *Annales Geophysicae*, 27, pp. 2607-2622, doi:
527 10.5194/angeo-27-2607-2009.

Formatted: Portuguese (Brazil)

528
529 Abdu, M. A., Brum, C. G. M., Batista, P. P., Gururbaran. S., Pancheva, D., Bageston, J. V.,
530 Batista, I. S., Takahashi, H. (2015). Fast and ultrafast Kelvin wave modulations of the equatorial
531 evening F region vertical drift and spread F development. *Earth, Planets and Space*, 67, pp. 1-15,
532 doi: 10.1186/s40623-014-0143-5.

Formatted: English (United States)

533
534 ..Basu, S. and S. Basu (1981). Equatorial scintillations - a review, *Journal of Atmospheric and*
535 *Terrestrial Physics*, 43 (5-6), pp. 473-489, doi:10.1016/0021-9169(81)90110-0.

536
537 Blewitt, G. (1990). An automatic editing algorithm for GPS data. *Geophysical Research Letters*,
538 [17\(3\), pp. 199-202](#), doi:10.1029/GL017i003p00199.
539
540 DasGupta, A., S. Ray, A. Paul, P. Banerjee, Bose, A. (2004), Errors in position-fixing by GPS in
541 an environment of strong equatorial scintillations in the Indian zone, *Radio Sci.*, 39, RS1S30,
542 doi:10.1029/2002RS002822.
543
544 de Paula E. R., Jonah O. F., Moraes A. O., Kherani E. A., Fejer B.G., Abdu M. A., Muella M. T.
545 A. H., Batista I. S., Dutra S.L. G., Paes R. R. (2015) Low-latitude scintillation weakening during
546 sudden stratospheric warming events. *J. Geophys. Res.*, 120, pp. 2212-2221, doi:
547 10.1002/2014JA020731.
548
549 Doherty, P. H., Delay, S. H., Valladares, C. E., Klobuchar, J. A. (2004). Ionospheric
550 Scintillation Effects on GPS in the Equatorial and Auroral Regions. *J. Inst. of Navig.*, 50(4), pp.
551 235-246, doi: 10.1002/j.2161-4296.2003.tb00332.x.
552
553 El Ayadi, M. M. H. and Ismail, M. H. (2014). Novel Closed-Form Exact Expressions and
554 Asymptotic Analysis for the Symbol Error Rate of Single- and Multiple-Branch MRC and EGC
555 Receivers Over α - μ Fading. *IEEE Trans. Veh. Technol.*, 63 (9), pp. 4277-4291, doi:
556 10.1109/TVT.2014.2316418.
557
558 Gao, Y. and X. Shen (2002). A New Method for Carrier-Phase-Based Precise Point Positioning.
559 *J. Inst. of Navig.*, 49 (2), pp. 109-116, doi: 10.1002/j.2161-4296.2002.tb00260.x.
560
561 Humphreys, T. E., Psiaki, M. L., Hinks, J. C., O'Hanlon B., Kintner, P. M. (2009). Simulating
562 Ionosphere-Induced Scintillation for Testing GPS Receiver Phase Tracking Loops. *IEEE J Sel*
563 *Top Signal Process*, 3 (4), pp. 707-715, doi: 10.1109/JSTSP.2009.2024130.
564

565 Humphreys, T. E., Psiaki, M. L., Ledvina, B. M., Cerruti, A. P., Kintner, P. M. (2010a). Data-
566 Driven Testbed for Evaluating GPS Carrier Tracking Loops in Ionospheric Scintillation. IEEE
567 Trans Aerosp Electron Syst, 46 (4), pp. 1609-1623, doi: 10.1109/TAES.2010.5595582.
568

569 Humphreys, T. E.; Psiaki, M. L. and P. M. Kintner, Jr. (2010b). Modeling the Effects of
570 Ionospheric Scintillation on GPS Carrier Phase Tracking. IEEE Trans. Aerosp. Electron.
571 Syst., 46 (4), pp. 1624-1637, doi: 10.1109/TAES.2010.5595583.
572

573 Kintner, P. M., Kil, H., Beach, T. L., de Paula, E. R. (2001), Fading timescales associated with
574 GPS signals and potential consequences, Radio Sci., 36(4), 731-743,
575 doi:10.1029/1999RS002310.
576

577 Kintner, P. M., Ledvina, B. M., de Paula, E. R. (2007). GPS and ionospheric scintillations. Space
578 Weather, 5 (S09003), pp. 1-23, doi:10.1029/2006SW000260.
579

580 Marques, H. A., Monico, J. F. G., Shimabukuro, M. H., Oyama, R. T., Wentz, J. P. (2014). Real
581 Time PPP: Fundamentals, Computational Implementation and Results Analysis for Static and
582 Kinematic Mode. Brazilian Cartography Magazine (Revista Brasileira de Cartografia), 6 (66),
583 pp. 1331-1345, ISSN: 1808-0936.
584

585 Marques, H. A. S., Monico, J. F. G., Marques, H. A. (2016). Performance of the L2C civil GPS
586 signal under various ionospheric scintillation effects. GPS Solut., 20 (2), pp. 139-149,
587 doi:10.1007/s10291-015-0472-2.
588

589 Moraes, A. O., de Paula, E. R., Perrella, W. J. Rodrigues, F. S. (2012). On the distribution of
590 GPS signal amplitudes during the low-latitude ionospheric scintillation. GPS Solut., 17 (4), pp.
591 499-510, doi:10.1007/s10291-012-0295-3.
592

593 Moraes, A. O., de Paula, E. R., Muella, M. T. A. H., Perrella, W. J. (2014a). On the second order
594 statistics for GPS ionospheric scintillation modeling. Radio Sci., 49 (2), pp. 94-105,
595 doi:[10.1002/2013RS005270](https://doi.org/10.1002/2013RS005270).

596
597 *Moraes, A. O., Costa, E., de Paula, E. R., Perrella, W. J., Monico, J. F. G. (2014), Extended*
598 *ionospheric amplitude scintillation model for GPS receivers, Radio Sci., 49, 315–333,*
599 *doi:10.1002/2013RS005307.*
600
601 *Moraes, A. O., Costa, E., Abdu, M. A., Rodrigues, F. S., de Paula, E. R., Oliveira, K., Perrella,*
602 *W. J. (2017), The variability of low-latitude ionospheric amplitude and phase scintillation*
603 *detected by a triple-frequency GPS receiver, Radio Sci., 52, 439–460,*
604 *doi:10.1002/2016RS006165.*
605
606 Moreno, B., Radicella, S., De Lacy, M. C., Herraiz, M. Rodriguez-Caderot, G. (2011). On the
607 effects of the ionospheric disturbances on precise point positioning at equatorial latitudes. *GPS*
608 *Solut., 15(4), pp. 381-390, doi:10.1007/s10291-010-0197-1.*
609
610 Magableh, A. M. Matalgah, M. M. (2009). Moment generating function of the generalized $\alpha - \mu$
611 distribution with applications. *IEEE Comm. Let., 13 (6), pp. 411-413, doi:*
612 *10.1109/LCOMM.2009.090339.*
613
614 Sobral, J. H. A., Abdu, M. A., Takahashi, H., Taylor, M. J, de Paula, E. R., Zamlutti, C. J.,
615 Aquino, M. G., Borba, G. (2002). Ionospheric plasma bubble climatology over Brazil based on
616 22 years (1977-1998) of 630 nm airglow observations. J. Atmos. Sol. Terr. Phys., 64 (12-14), pp.
617 1517-1524, doi: 10.1016/S1364-6826(02)00089-5.
618
619 Ray, S., Bhowmik, U., and Das, A. (2014), Scintillation effects related to propagation geometry
620 as applicable to Indian SBAS, Proceedings of the XXXI URSI General Assembly and Scientific
621 Symposium, paper 1463, Beijing, China.
622
623 Teunissen, P. J. G. (1998). Quality control and GPS. In: Teunissen, P. J. G., Kleusberg, A. (eds.),
624 GPS for geodesy, 2nd ed. Springer, Berlin, pp 271–318.

Formatted: English (United States)

625 Tsunoda, R. T. (1985). Control of the seasonal and longitudinal occurrence of equatorial
626 scintillations by the longitudinal gradient in integrated E region Pederson conductivity. J
627 Geophys Res., 90 (A1), pp. 447-456, doi: 10.1029/JA090iA01p00447.

628
629 Thébaud, E.; et al. (2015). [International Geomagnetic Reference Field: the 12th generation](#).
630 Earth, Planets and Space, 67:79, pp. 1-19, doi: 10.1186/s40623-015-0228-9.

631
632 [Vani, B. C., Shimabukuro, M. H. Monico, J. F. G. \(2016\). Visual exploration and analysis of](#)
633 [ionospheric scintillation monitoring data: The ISMR query tool. Comp. & Geosc., 104, pp.125-](#)
634 [134, doi: 10.1016/j.cageo.2016.08.022.](#)

Formatted: Portuguese (Brazil)

635
636 Xu, R., Liu, Z., Li, M., Morton, Y., Chen, W. (2012). An analysis of low-latitude ionospheric
637 scintillation and its effects on precise point positioning. Journal of Global Positioning Systems,
638 11(1). Pp. 22-32, doi: 10.5081/jgps.11.1.22.

639
640 Yacoub, M. D. (2007). The α - μ distribution: A physical fading model for the Stacy distribution.
641 IEEE Trans Veh Technol, 56 (1), pp. 27-34, doi:10.1109/TVT.2006.883753.

642
643 Yeh, K. C. and Liu, C. H. (1982). Radio wave scintillations in the ionosphere, Proceedings of the
644 IEEE, 70 (4), pp. 324-360, doi:10.1109/PROC.1982.12313.

645
646 Zhang, X., Guo, F., Zhou, P. (2014). Improved precise point positioning in the presence of
647 ionospheric scintillation. GPS Solut, 18 (1), pp. 51-60, doi:10.1007/s10291-012-0309-1.

648
649 [Zumberge, J. F., Heflin, M. B., Jefferson, D. C., Watkins, M. M., Webb, F. H. \(1997\). Precise](#)
650 [point positioning for the efficient and robust analysis of GPS data from large networks. J](#)
651 [Geophys Res., 102 \(B3\), pp. 5005-5017, doi: 10.1029/96JB03860.](#)

Formatted: English (United States)

652
653 **Author Biographies**
654 **Alison Moraes** received the B.S. in telecommunications engineering from Universidade de Taubaté,
655 UNITAU, Brazil in 2003, and Dr. Sc degree in the school of Electronic and Computer Engineering at

656 Instituto Tecnológico de Aeronáutica, ITA, Brazil in 2013. Engineer at the Instituto de Aeronáutica e
657 Espaço IAE since 2004, and graduate professor at ITA since 2015.

658

659 **Bruno Vani:** Received the B.S. in Computer Science (2011) and M. Sc. (2014) in Cartographic Sciences
660 from Univ. Estadual Paulista (UNESP). Currently he is a PhD candidate at UNESP. Since 2014, he is a
661 lecturer at the Instituto Federal de São Paulo (IFSP/SP), Presidente Epitácio, Brazil.

662

663 **Emanuel Costa:** received the BS and MS degrees in electrical engineering from Instituto Militar de
664 Engenharia, Brazil in 1972 and 1974, and the Ph. D. degree from Cornell University, USA, in 1978. He
665 has been with CETUC/PUC-Rio, Brazil, since 1978, with research interests in the areas of tropospheric
666 and ionospheric effects on radio wave propagation.

667

668 **Mangalathayil Abdu:** Received Ph.D. degree, in 1967, from Gujarat University India. He has been
669 postdoctoral research fellow at the University of Western Ontario (1968- 71), professor at CRAAM
670 Mackenzie University, Sao Paulo (1971-73), research scientist since 1973 at the National Institute for
671 Space Research (INPE), and presently a visiting professor at ITA. His research interests are in space
672 weather and Ionospheric physics..

673

674 **Eurico de Paula:** attended the M. Sc. degree at Telecommunications at ITA, and Dr. Sc. in Geophysics at
675 INPE, where he has been working as a Researcher for 40 years. He attended pos-doc programs at USU,
676 Utah State University, Logan, USA for 5 years. His main area of interest is ionospheric physics with
677 focus on ionospheric scintillations detected by radars and GPS receivers.

678

679 **Jonas Sousasantos:** Graduated in Mathematics at the Universidade de Taubaté, UNITAU, Brazil in
680 2010. Dr. Sc. (2017) and M. Sc. (2013) degrees obtained at the National Institute for Space Research. He
681 is currently a Postdoctoral Associate at Instituto Tecnológico de Aeronáutica, ITA. His main area of
682 interest is mathematical modeling and forecasting of ionospheric irregularities and atmospheric-
683 ionospheric vertical coupling.

684

685 **Galera Monico:** Graduated in Cartographic Eng. from UNESP (1982), master in Geodetic Science from
686 UFPR (1988) and Ph.d. on Space Geodesy from Nottingham University (1995). Has experience in
687 Geosciences, focusing on the following subjects: GNSS for Geodesy and Atmosphere, Quality Control on
688 Geodesy. Dr. Galera Monico was indicated as one of the 50 GNSS Leaders to Watch by the GPS World
689 magazine.

690

691 **Biagio Forte:** Dr graduated in Physics at the University of Trieste (Italy) and went on to complete a PhD
692 in Geo-Physics at the Karl-Franzens University of Graz (Austria). Biagio joined the Department of
693 Electronic and Electrical Engineering in 2012 as a Prize Fellow in Space Weather.

694

695 **Patricia Negreti:** Graduated in Physics from Universidade Estadual Paulista Júlio de Mesquita Filho
696 (2003), where he received 4 awards/honors. Masters in Medical Physics by the Institute of Energy and
697 Nuclear Research (2006) and PhD in Space Geophysics by the National Institute of Space Research
698 (2012).

699

700 **Milton Shimabukuro:** Assistant Professor at UNESP, Presidente Prudente, São Paulo, Brazil, since
701 2006. He received B.S. degree in Computer Science and doctorate in Computer Science and
702 Computational Mathematics, both from Institute of Mathematics and Computer Sciences, University of
703 São Paulo, Brazil. His research interests are visual analytics, organization and visualization of spatial and
704 temporal data.